

Optimization of the Eddy Current Testing

Hiroki KIKUCHIHARA¹, Iliana MARINOVA², Yoshifuru SAITO¹,
Manabu OHUCH³, Hideo MOGI³ and Yoshiro OIKAWA³

¹ Graduate School of Hosei University, Tokyo 184-8584, Japan

² Technical University of Sofia, Sofia 1756, Bulgaria

³ Denshijiki Industry Co., Ltd, Tokyo 115-0051, Japan

Eddy current testing (ECT) is one of the most representative nondestructive testing methods for metallic materials, parts, structures and so on. Operating principle of ECT is based on the two major properties of magnetic field. One is that alternating magnetic field induces eddy current in all of the conducting materials. Thereby, an input impedance of the magnetic field source, i.e., electric source, depends on the eddy current path. Second is that the magnetic field distribution depends only on the exciting but also the reactive magnetic fields caused by the eddy currents in targets. Former and latter are the impedance sensing and magnetic flux sensing types, respectively.

This paper concerns with an optimization of a new magnetic flux sensing type sensor named " ∞ coil" whose exciting and sensing coils are composed of the ∞ shape and finite length solenoid coil wound ferrite bar, respectively. Development of this ∞ coil fully depends on the 2D and 3D finite elements methods. According to the simulation results, we have worked out two types of ∞ coils. Practical experiments reflect on the validity of both simulation and design aims, quite well.

Index Terms— Eddy current, Nondestructive testing

I. INTRODUCTION

Modern engineering products such as air-plane, automobile, smart building, high speed train and so on are essentially composed of metallic materials for forming the shape of product, suspending the mechanical stress and constructing the structural frames. In particular, the mass transportation vehicles, e.g. large air plane, high-speed train, express highway bus and so on, carrying a large number of people are required ultimately high safety as well as reliability. To keep the safety, nondestructive testing to the metallic materials is one of the most important technologies because most of the structure materials are composed of the metallic materials.

Various nondestructive testing methods, such as eddy current testing (ECT), electric potential method, ultrasonic imaging and x-ray tomography, are currently used. Among these methods, ECT needs not complex electronic circuits and direct contact to target. Furthermore, a target whose major frame parts are composed of conductive metallic materials can be selectively inspected by ECT [1,3].

In this paper, a new ECT sensor coil named " ∞ coil" is proposed. Development of this ∞ coil fully depends on the 2D and 3D finite elements methods and optimize and the eddy current testing.

The most important key idea of the ∞ coil is that setting the sensor coil in the lowest magnetic field space caused by the exciting coils, because this sensor coil is capable of catch only the magnetic fields caused by the detour eddy currents flowing around a defect. This paramount important key idea has been yields intensive 2D finite elements simulation. After that 3D finite elements simulation has been carried out to check up the validity of this key idea.

Thus, we have succeeded in innovating and optimizing a new high sensibility eddy current sensor " ∞ coil" by means of the 2D and 3D finite elements simulations [2,3].

II. NEW ECT SENSOR COIL

1) Operating principle of ECT

Operating principle of the separately installed sensing coil type is fundamentally based on that the sensing coil catches the magnetic field intensity variation caused by the detour eddy currents flowing around a defect in the target metallic materials.

To realize this, three methodologies may be considered. The first detects the variation of entire magnetic fields caused by both exciting and eddy currents. In this case, the sensing coil detects the magnetic fields distribution caused by the detour eddy currents around defects among the entire magnetic fields. Second is that the sensing coil surface is installed in a perpendicular direction to an exciting coil surface. This means that the sensing coil never induce an electric voltage caused by the exciting fields because the surface of sensing coil always parallels to the exciting magnetic fields, so that this sensing coil is capable of selectively catching the magnetic fields caused by the detour eddy currents around a defect. This type of sensor has high liftoff characteristics compared with those of the first one. The final third one is that the sensing coil is set on the zero exciting magnetic fields space in addition to the second one coil layout. This final one is capable of catching only the magnetic fields caused by the detour eddy currents around a defect, and has been innovated in this paper by a sequential intensive finite elements simulation.

2) 2D simulation

At the beginning of our new sensor project, to concentrate the magnetic fields, as shown in Fig.1, the two exciting coils whose magneto motive forces becomes in additive were employed.

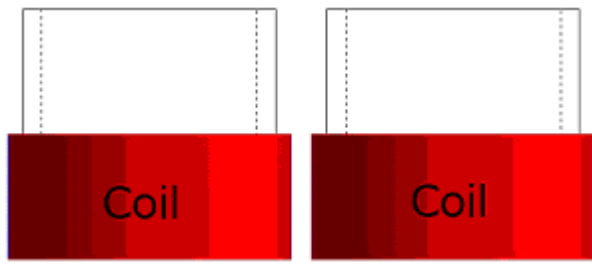
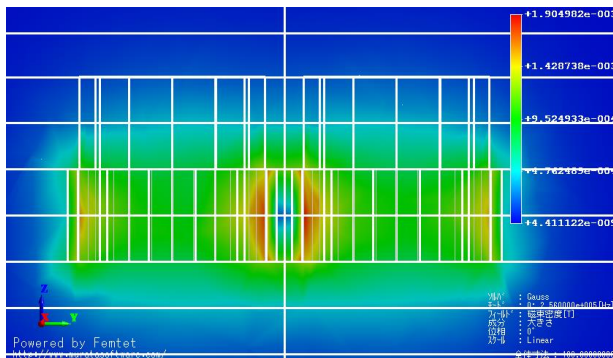


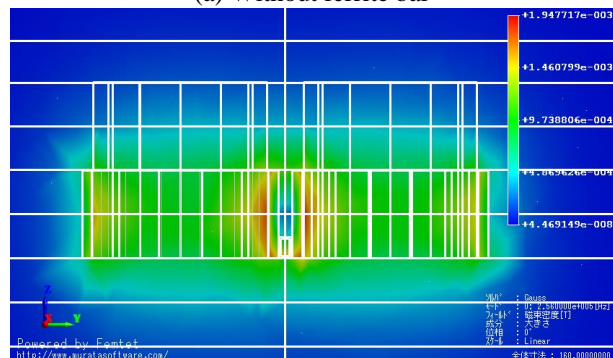
Fig.1 Two exciting coils

To decide a location of sensing coil whose surface is orthogonal to the exciting magnetic fields, we have carried out a lot of 2D finite elements simulations. As a result, it is found that there is nearly zero exciting fields space between the two exciting coils. This leads to our ∞ coil. Since the zero exciting magnetic fields condition in addition to the orthogonal coil surface layout to the exciting magnetic fields enhances the sensibility of ∞ coil in an ultimately.

Fig 2(a) shows an exciting magnetic field intensity distribution. In this figure, it is possible to find the zero magnetic fields space between the two parallel exciting coils. According to this simulation result, we put on a ferrite bar at the bottom surface of the two exciting coils in order to enhance the sensibility of sensor coil. As shown in Fig.2(b), setting the ferrite bar hardly disturb the exciting magnetic fields intensity distribution. Thus, winding around the sensor coil around the ferrite core leads to an ultimately optimized high sensibility ECT sensor, i.e., ∞ coil.



(a) Without ferrite bar



(b) With ferrite bar

Fig. 2 Magnetic fields intensity

3) 3D simulation of the ∞ coil

To evaluate and validity check of the ∞ coil performance, we employed a 3D simulation model shown in Fig.3.

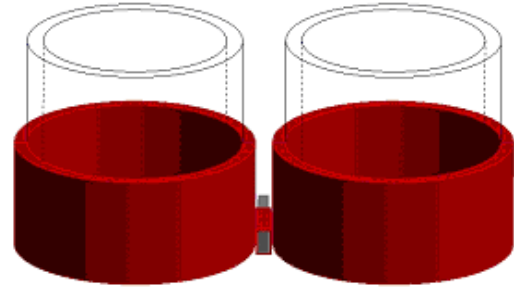
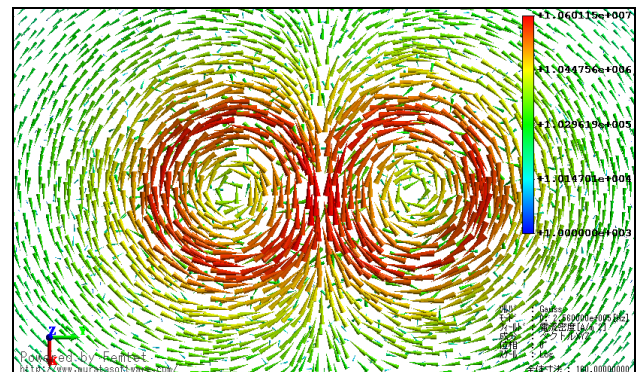


Fig.3 3D simulation model of the ∞ coil

Table 1 various constants used in the 3D simulation.

Exciting coil	
Coil outer diameter	22.4mm
Coil inner diameter	20mm
Coil length	10mm
Number of turn	75
Input current(peak)	250mA
Frequency	256kHz
Sensing coil	
Coil outer diameter	1.4mm×2.4mm
Coil inner diameter	1mm×2mm
Coil length	6mm
Number of turn	100
Axis core	JFEferrite_MB1H_23°C

Table 1 lists various constants used in the 3D simulation. The eddy currents in a plane target located under the two exciting coil surfaces are shown in Fig. 4, where the two adjacent exciting coils side to the no-defect, 0 degree, 90 degree and 45 degree line defects are shown in Figs. 4(a),4(b),4(c) and 4(d), respectively.



(a) No defect

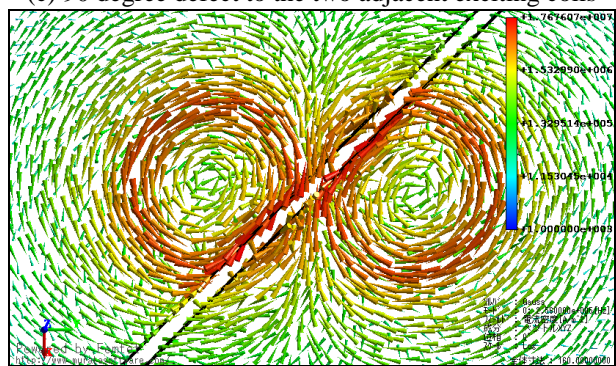
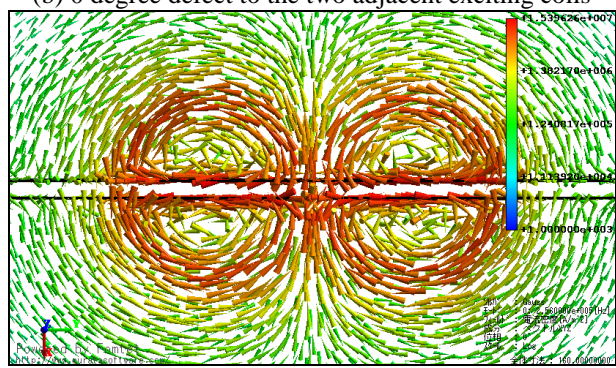
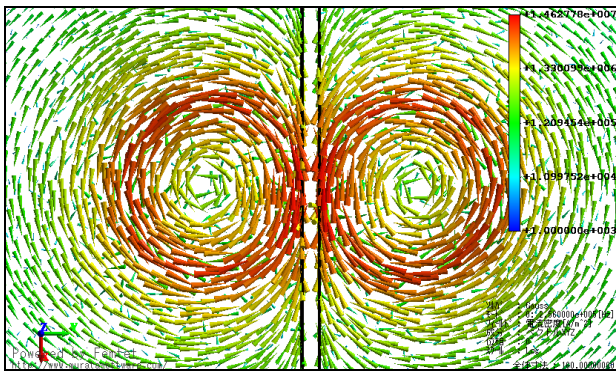


Fig.4 Eddy currents in a plane metallic target.

Fig.5 shows the magnetic flux density vector distribution corresponding to that of eddy currents in Fig. 4. Observe the magnetic flux density vector distributions in Fig.5 reveals that the sensing coil wound around the ferrite bar could be induced the electric voltages not the cases (a), (b), (c) and (d).

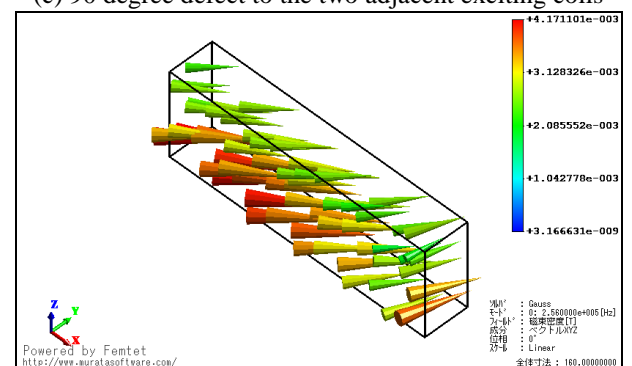
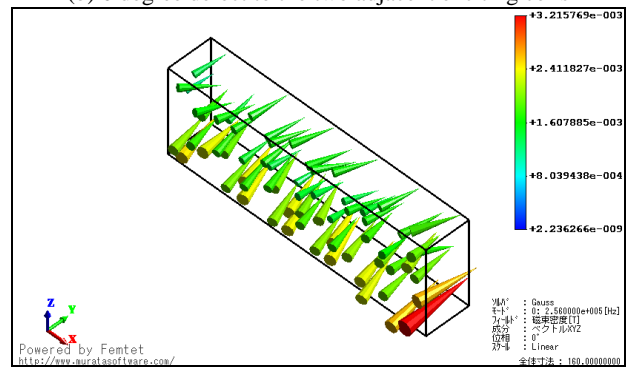
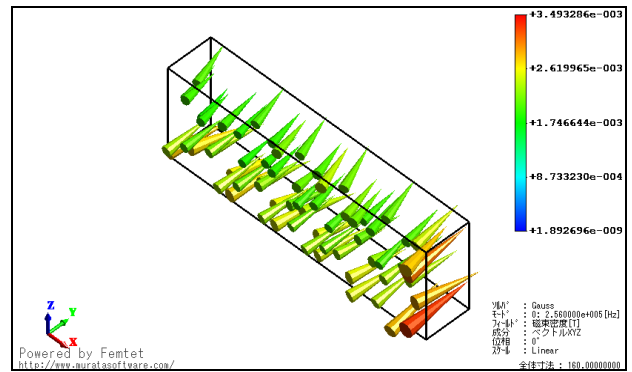
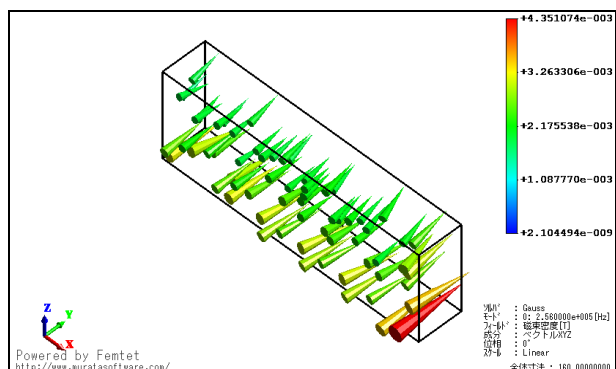


Fig.5 Magnetic flux density vector distributions in the ferrite bar

The induced voltages of the sensor coil under the conditions (a)-(d) in Figs.4 and 5 are shown in Fig.6. By observing the induced voltages in Fig.6 reveals that the case (d) yields the highest voltage.



(a) No defect

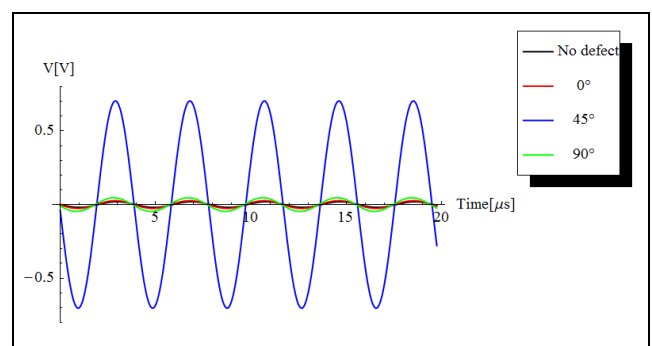


Fig.6 Induced voltages in the sensor coil

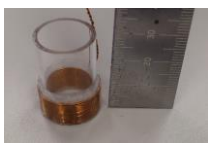
III. EXPERIMENT

1) Tested target piece and ∞ coil

We employed two copper plates having 1mm thickness as target metal plates. One has no defect and the other has a line defect having 2mm width. Also, we worked out a prototype of the ∞ coil. Table 2 lists various constants of the prototype ∞ coil. We used two exciting coils and one sensing coil having ferrite core. Fig. 7 shows a picture of the prototype ∞ coil. The physical dimensions of this prototype ∞ coil are corresponding to the 3D simulation model shown in Fig.3.

Table 2 Various constants of the prototype ∞ coil.

Exciting coil	
Conductor length	4.7m
Diameter of conductor	0.4mm
Coil outer diameter	23mm
Coil inner diameter	20mm
Coil length	10mm
Number of turn	75
Number of coil layers	3
Number of coils	2



Sensing coil	
Conductor length	60cm
Diameter of conductor	0.1mm
Axis core	Ferrite bar (MnZn)
Coil outer diameter	1.4mm×2.4mm
Coil inner diameter	1mm×2mm
Coil length	6mm
Number of turn	100
Number of coil layers	2

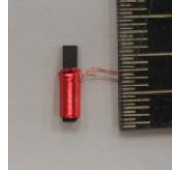



Fig.7 Picture of the prototype ∞ coil.

2) Experimental results

Fig.8 shows the measured voltages corresponding to that of cases in Figs. 4 and 5. Even though the peak measured voltage is somewhat smaller than those of Fig.6, sensing characteristics of the prototype ∞ coil are well corresponding to that of Fig. 6.

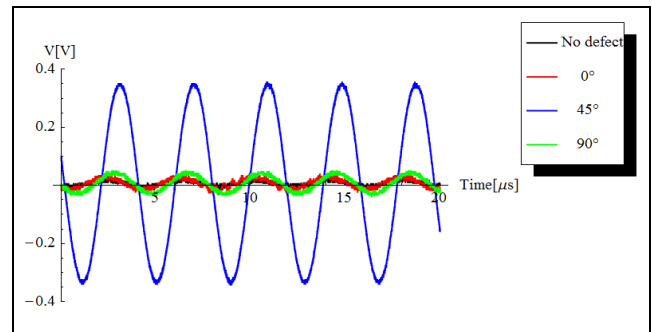


Fig.8 Measured voltages of the practical sensing coil.

IV. CONCLUSION

As shown above, we have succeeded in innovating and optimizing a new high sensibility eddy current sensor " ∞ coil" by means of the 2D and 3D finite elements simulations.

Thus, we have elucidated that the finite elements simulation technology is one of the most effective and powerful tools to research and develop the new electromagnetic devices. All of the 2D and 3D finite elements simulations were carried out by the finite element package "femtet" produced by Murata Software Co. Ltd.

REFERENCES

- [1] I.Marinova, S.Hayano and Y.Saito, Ployphase eddy current testing, Journal of Applied Physics, Vol. 75, No.10, pp. 5904-5906, 1994.
- [2] N.Burais and A.Nicolas, Electromagnetic field analysis in remote field eddy current testing systems, IEEE Transactions on Magnetics, Vol.25, No.4, pp.3010-3012, 1989.
- [3] S.McFee and J.P.Webb, Automatic mesh generation for h-p adaption, IEEE Transactions on Magnetics, Vol.29, No.2, pp.1894-1897, 1993.

Fluctuation Frequency Analysis of the Barkhausen Signals under Static and Dynamic Stresses

Jun KAWAZOE¹, Iliana MARINOVA², and Yoshifuru SAITO¹

¹ Graduate School of Hosei University, Tokyo 184-8584, Japan

² Technical University of Sofia, Sofia 1756, Bulgaria

Ferromagnetic materials are widely used for various artificial products such as cars, trains, ships and so on. Because of its mechanical property, iron steel is most popular in use for frame materials. Nondestructive testing of iron steel is an extremely important way to maintain their mechanical reliability. As is well known fact, the Barkhausen signals are emitted from only the ferromagnetic materials having magnetic domain structures. Also this signal varies depending upon their past mechanical as well as radioactive stress histories.

In the present paper, we have applied a generalized frequency fluctuation analysis to the Barkhausen signals to detect the various mechanical stresses. Surprisingly, it has been succeeded in clarifying that application of our frequency fluctuation analysis to the Barkhausen signals makes it possible to detect the two kinds of mechanical stress.

Index Terms—Barkhausen signal, Frequency fluctuation, Signal processing, Least squares

V. INTRODUCTION

Barkhausen signal is popularly observed in the ferromagnetic materials composed of the magnetic domain structures, e.g. iron, nickel, cobalt and garnet, when they are magnetizing. Also, it is well known that the Barkhausen signals are very sensitive to the physical external input, such as mechanical stress and radioactive damage, to the ferromagnetic materials [1].

According to the past researches concerning to a relationship between the Barkhausen signal and applied mechanical stress, it has been revealed that Barkhausen signals are very sensitive to the mechanical stress and radioactive damage but any deterministic regularity has not been found.

Recently, only a macroscopic regularity has been reported by means of a 1st order frequency fluctuation analysis approach [2]. Principal purpose of this paper is that conventional frequency fluctuation analysis employing only 1st order fluctuation is generalized to the frequency fluctuation analysis employing the n^{th} order fluctuations.

As a result, we succeed in extracting the distinct difference between the stressed and not stressed Barkhausen signals. Also, we succeed in visualizing in the most clear manner on the four dimensional space, whose coordinates are composed of the terms representing the higher order frequency fluctuation terms of Barkhausen signals.

One of the most famous frequency fluctuations is the 1/f frequency fluctuation, which can be observed in most of the natural phenomena such as natural wind, sea water waves, river flow sound and so on gives a healing effect to the mentalities via human sensibilities [3].

Conventional 1/f frequency analysis is that application of the 1st order least squares to the both Fourier power spectrum and frequency extracts the 1st order frequency fluctuation, i.e., Log of Fourier power spectrum is approximated by Log of $a_0 + a_1f$, yields a 1st order frequency fluctuation characteristic,

where a_0 and a_1 are the 0th and a 1st order frequency fluctuation terms, respectively. If the frequency fluctuation term a_1 takes $a_1=1$, then we have the 1/f frequency fluctuation.

On the other side, we generalize this conventional 1st order frequency fluctuation to the n^{th} order frequency fluctuation characteristics, i.e., Log of Fourier power spectrum is approximated by a Log of $a_0 + a_1f + a_2f^2 + \dots + a_nf^n$, where $a_0, a_1, a_2, \dots, a_n$ are the 0th, 1st, 2nd, ... , n^{th} order frequency fluctuation terms, respectively. Careful examination of the coefficients $a_0, a_1, a_2, \dots, a_n$ leads to the precise frequency fluctuation characteristic of the Barkhausen signal.

Second important key point of our approach is how to visualize the dependency of the 0th, 1st, 2nd, ... , n^{th} order frequency fluctuation terms to the externally applied forces.

According to our experimental results on this research, most of the frequency fluctuation characteristics are sufficiently represented up to the 4th order terms. So that let the normalized 1st, 2nd, 3rd, 4th order frequency fluctuation coefficients be respectively the coordinate values on the x-, y-, z-axes, and point color, then up to the 4th order frequency fluctuation characteristics locate the three dimensional space coordinate position and point color. Thus, comparison among the different specimens of this diagram visualizes an each of the distinct characteristics depending on their mechanical stress conditions.

VI. FREQUENCY FLUCTUATION ANALYSIS

1) Basic equations

Let us consider an arbitrary signal $g(t)$ and its Fourier power spectrum $G(f)$, and take the logarithm of both Fourier spectrum $G(f)$ and frequency f . Plot the $\log G(f)$ on the $\log f$ coordinate represents a frequency characteristic of the signal $g(t)$ on the frequency domain, i.e., the frequency characteristic of the original signal is represented on a x-y plane coordinate system whose horizontal x- and vertical y-axes are

corresponding to the logarithms of Fourier power spectrum $G(f)$ and of frequency f , respectively.

In order to represent a global frequency characteristic of the original signal $g(t)$ in frequency domain, apply a following power series function:

$$h(f) = a_0 + a_1 f + a_2 f^2 + \dots + a_n f^n. \quad (1)$$

This x - y plane makes it possible to evaluate the higher order frequency fluctuation analysis. The coefficients $a_0, a_1, a_2, \dots, a_n$ in (1) are determined by least squares as

$$\mathbf{A} = [\mathbf{C}^T \mathbf{C}]^{-1} \mathbf{C}^T \mathbf{Y}. \quad (2)$$

A superscript T denotes a matrix transpose; the vectors \mathbf{A} , \mathbf{Y} and matrix \mathbf{C} are respectively given by

$$\mathbf{A} = [a_0 \quad a_1 \quad \dots \quad a_n]^T, \quad (3)$$

$$\mathbf{Y} = [h(f_0) \quad h(f_1) \quad \dots \quad h(f_m)]^T, \quad (4)$$

$$\mathbf{C} = \begin{bmatrix} 1 & f_0 & f_0^2 & \dots & f_0^n \\ 1 & f_1 & f_1^2 & \dots & f_1^n \\ \vdots & \vdots & \vdots & \dots & \vdots \\ 1 & f_m & f_m^2 & \dots & f_m^n \end{bmatrix}, \quad (5)$$

$$m > n.$$

In (3)-(5), a number of equations m , i.e. number of the sampled frequencies $f_0, f_1, f_2, \dots, f_n$, always greater than those of unknowns n , i.e., number of the coefficients $a_0, a_1, a_2, \dots, a_n$. In most case, this condition is satisfied because of the number of sampled frequency m is much greater than those of the order n of the function $h(f)$ in (1).

2) Classical 1st order frequency fluctuation

Fig. 1 shows a Barkhausen signal measurement devices. The tested specimens are the silicon steels with the 0.35mm thickness, 30mm width and 100mm length. The tested specimen is put on the upper two head surfaces of U shape ferrite core wound the 300 turns exciting coil. The specimen in Fig.1 is excited by flowing a 1A sinusoidal alternating current through this exciting coil.

Fig. 2 shows a typical frequency characteristic of a Barkhausen signal under no stress.

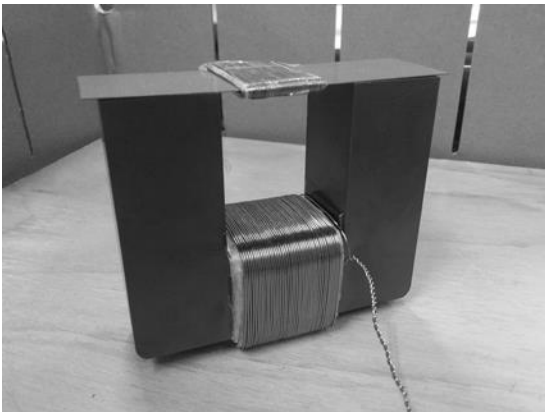


Fig. 1. Barkhausen signal measurement devices.

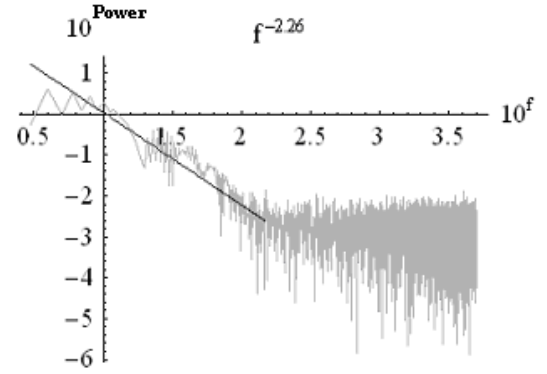


Fig. 2. An example of typical frequency characteristic of a Barkhausen signal under no stress.

The frequency characteristic in Fig. 2 is obviously divided into two frequency regions. One is lower frequency region whose frequency fluctuation can be approximated by $f^{-2.26}$ derived from 1st order approximation in (1), and the other higher one is a dispersing signal whose frequency fluctuation can be approximated by f^0 , i.e. white noise.

On the other side, Fig. 3 shows a typical frequency characteristic of Barkhausen signal under 3kg stressed.

The frequency characteristic in Fig. 3 is also divided into two frequency regions. One is lower frequency region whose 1st order frequency fluctuation can be approximated by $f^{-1.69}$, and the other higher one is a dispersing signal whose frequency fluctuation can be approximated by f^0 .

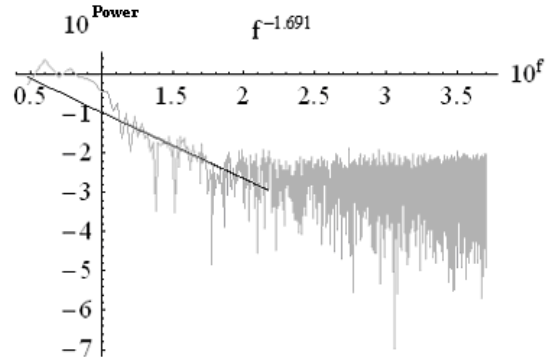


Fig. 3. An example of typical frequency characteristic of a Barkhausen signal under 3kg stressed.

Consideration of the difference between the first order frequency fluctuations $f^{-2.26}$ and $f^{-1.69}$ suggests that an application of the 3kg stress to the tested silicon steel changes the steep 1st order gradient -2.26 to the smoothly gradient -1.68. This result had been verified by the 1st order frequency fluctuation analysis of the 30 distinct sample specimens [2].

Thus, it is possible to detect the stress on the ferromagnetic materials by the classical 1st order frequency fluctuation analysis.

However, the difficulty is still remaining, i.e., how to decide the frequency range for which to be computed the frequency fluctuation characteristic. This problem is solved in this paper by employing one of the optimization methods: i.e., k-means method based on Euclid distance [4].

3) Stress visualization

We have carried out the random stresses visualization in much the same as described in Section 2.2. These stresses were applied to the specimen by handling the random weights by a string as shown in Fig. 4 while the specimen is fixed by wood blocks to keep the same flux path conditions.

Fig. 5 shows one of the frequency characteristic of the Barkhausen signals under stress. The frequency characteristic in Fig. 5 is also divided into the two frequency regions. One is lower frequency region and the other is higher one. The higher frequency region is a tendency same as white noise. Thereby it is essential to reduce influence of the higher one to judge under stress otherwise no stress.

Fig. 6 shows that Fig. 5 is divided into two groups by the k-means method based on Euclid distance [4].

In much the same way as the 1st order frequency fluctuation, the left side group is a meaningful frequency region. Thereby we have carried out the stresses visualization only applying the higher order frequency fluctuation analysis to this meaningful frequency region in Fig. 6. Because of too small coefficient of over 4th order terms, a frequency fluctuation characteristic under stress along with the meaningful frequency region is obtained by up to the 4th order power series function in (1). To check the reproducibility of the coefficients a_1, a_2, a_3, a_4 , we have 10~12 times independently measured and computed these coefficients a_1, a_2, a_3, a_4 in (1) to the same specimen. After normalizing all of the coefficients a_1, a_2, a_3, a_4 to be the values between 1 and 0, let the normalized coefficients a_1', a_2', a_3', a_4' be respectively corresponded to the x-, y-, z-axes values and point color, then this makes it possible to visualize a dispersion characteristic of the coefficients a_1', a_2', a_3', a_4' . Fig. 7 shows a dispersion characteristics of coefficients a_1', a_2', a_3', a_4' .

The magnitude of 4th order normalized frequency fluctuation coefficients in Fig. 7 is rainbow colored.

Fig. 8 shows the normalized frequency fluctuation coefficients in terms of the black and light gray colors. The black and light gray colors are corresponding to the specimens under no stress and stress, respectively.

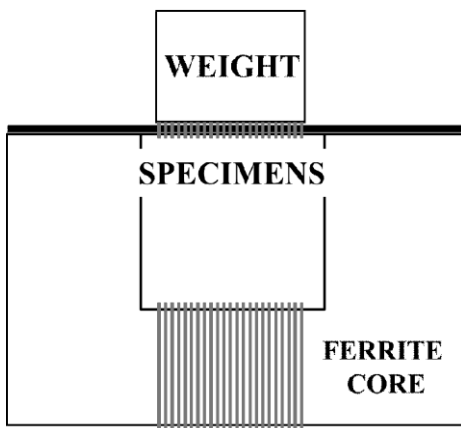


Fig. 4. The stresses are applied by hanging the weights.

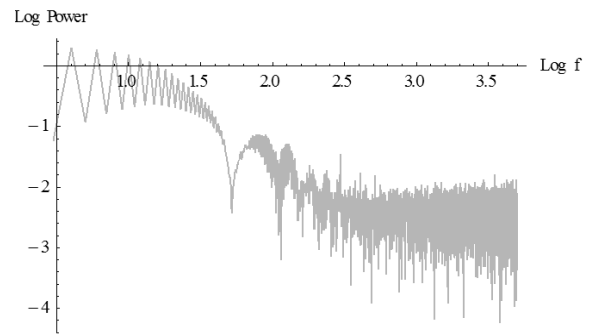


Fig. 5. One of the frequency characteristic of the Barkhausen signals under stress.

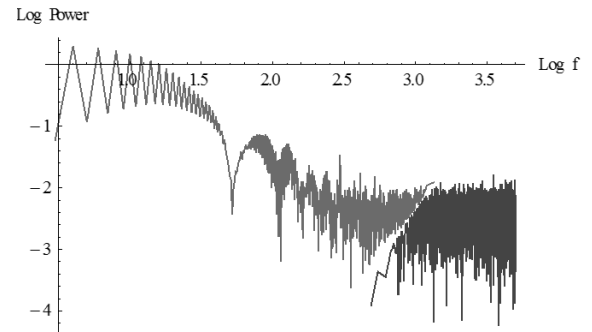
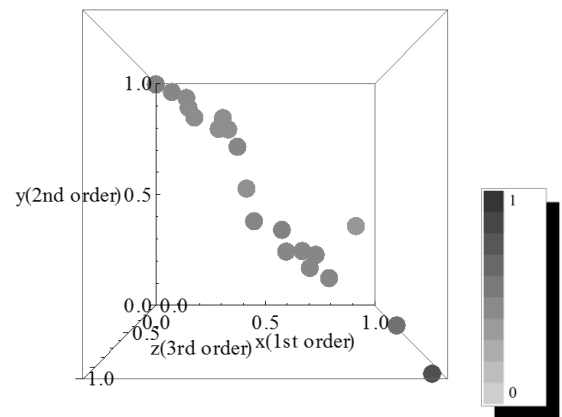
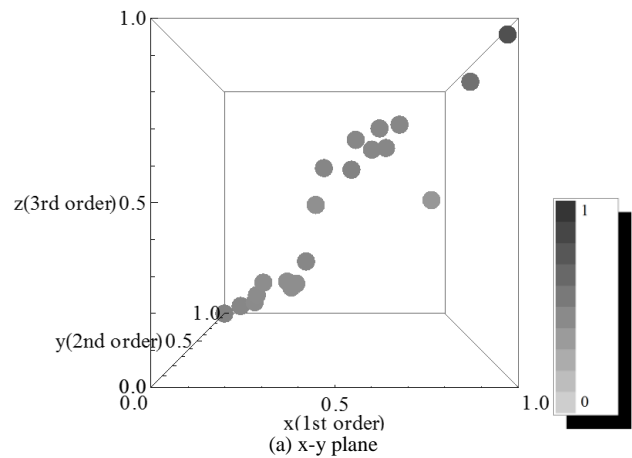


Fig. 6. Classified into two groups denoted light and dark colors by means of the k-means method based on Euclid distance.



(b) x-z plane

Fig. 7. The dispersion characteristics of coefficients.

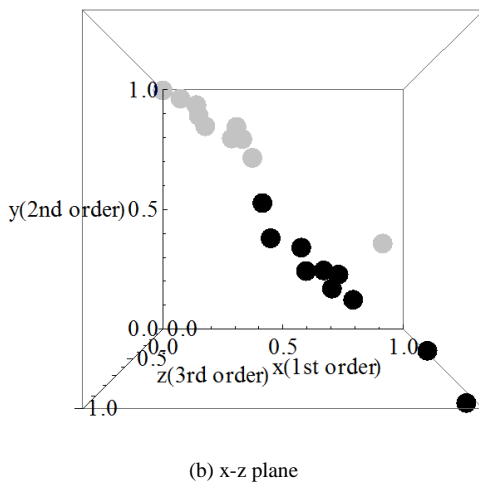
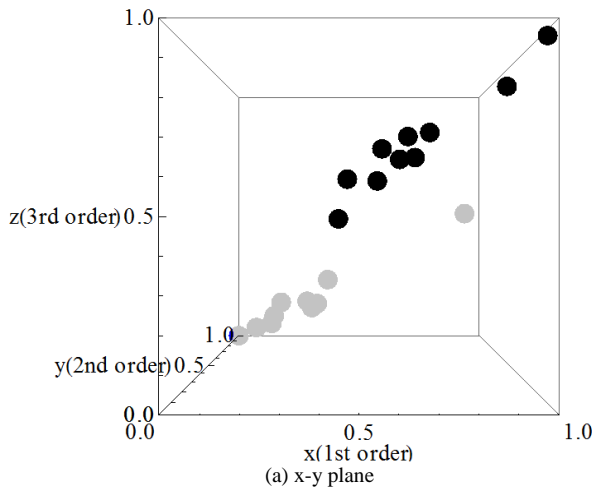


Fig. 8. The normalized frequency fluctuation coefficients difference between the stressed and no stressed groups.

The dispersion characteristics of coefficients divided in the stressed group and no stressed group in Fig. 8 are clustered by the k-means method based on Euclid distance as shown in Fig. 9.

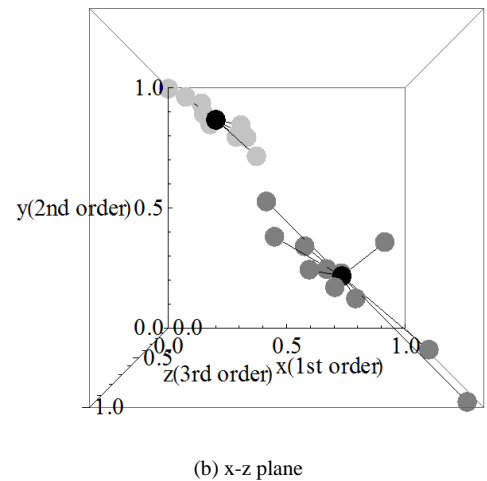
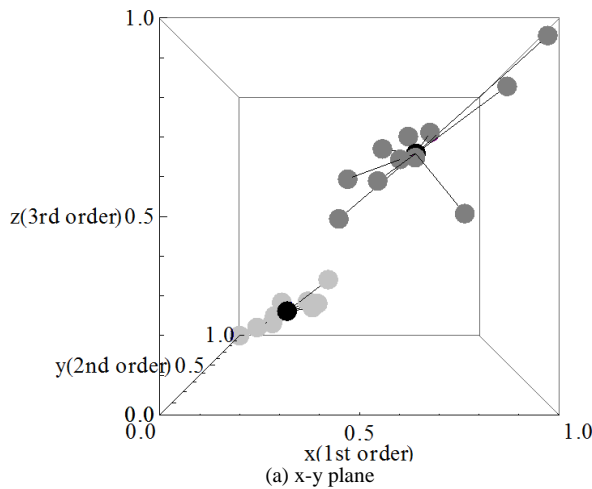


Fig. 9. Classified into two groups of the normalized frequency fluctuation coefficients difference between the stressed (light gray) and no stressed (dark gray) groups by means of the k-means method based on Euclid distance. The centroid of each of the 2 clusters is shown by a black point.

Observation of the dispersion characteristics of the stressed specimens suggests that the normalized coefficients a_1', a_2', a_3', a_4' in (1) do not disperse but focus on a relatively small area centered at (0.2,0.8,0.1). On the contrary, the normalized coefficients a_1', a_2', a_3', a_4' in (1) of the no stressed specimens disperse the vicinity of a centroid (0.6,0.2,0.6).

This means that the externally applied stress suppresses the dispersion and confines them into the small space in Fig. 9.

VII. CONCLUSION

Previously, we have succeeded in detecting the applied stress on the silicon steel by means of the 1st order frequency fluctuation method [2].

This paper has generalized this 1st order analysis method to the n^{th} order frequency fluctuations analysis method.

Up to the 4th order frequency fluctuation characteristics have been visualized in a three-dimensional space. Further it has been revealed that each of the distinct differences among the specimen not stressed and stressed is clarified by the k means method based on Euclid distance.

REFERENCES

- [4] R.M. Bozorth, Ferromagnetism, IEEE PRESS, p. 462, 1993.
- [5] S. Nojima and Y. Saito, Application of Frequency Fluctuation to Barkhausen Signals and its Application, J. Magn. Soc. Jpn., 35, 380-385, 2011.
- [6] M. Teranishi, K. Maruyama, S. Hayano, and Y. Saito: Visualization of 1/f Frequency Component in Dynamic Image of Natural Phenomena, The Visualization Society of Japan, B108, July, 2005.
- [7] J.B. MacQueen, Some Methods for classification and Analysis of Multivariate Observations, Proceedings of 5th Berkeley Symposium on Mathematical Statistics and Probability, University of California Press, pp. 281-297, 1967.

Optimization of the Secondary Resonant Contactless Transformer

Tatsuya OHASHI¹, Yoshifuru SAITO¹, and Iliana MARINOVA²

¹ Graduate School of Hosei University, Tokyo 184-8584, Japan

² Technical University of Sofia, Sofia 1756, Bulgaria

Contactless power supplier is composed of a transformer having the distinct primary and secondary coils separated by air gap. Because of the electromagnetic compatibility problem, it is essential to keep the leakage magnetic fields around the contactless power supplier as low as possible. Previously, we have reported that an application of the discrete wavelets transform to the magnetic field vector distributions around the transformer having open magnetic flux paths clarifies that the soup plate like ferrite cores embedding spirally wound coils gives a far excellent magnetic field vector distribution compared with those of the conventional U shape cores. As a result, we have succeeded in obtaining one of the reasonable core shapes by observing the wavelets spectra of measured magnetic field vector distributions. Furthermore, it has been revealed that a tested trial transformer gives nearly 80 percent power transmission efficiency even though the primary and secondary coils are separated by 10mm air gap. This paper is one of the success research solutions to overcome the specific absorption rate (SAR) problem based on the finite elements and optimization methodologies. Namely, a contactless flat shaped transformer whose primal and secondary ferrite cores are separated has been successfully optimized by combining the finite elements with linear programming optimization approaches.

Index Terms— contactless transformer, magnetic field visualization, SAR optimization

VIII. INTRODUCTION

Development of modern semiconductor technology makes it possible to realize the small and light weight electronic devices equipped with a large variety of smart functions such as smart cellular phone, ultra mobile computers, etc.

Although these electronics provide the highly efficient job environment, entertainments and convenient electronic consumer life, environments around human life are filling up with the electromagnetic fields. Particularly, because of the many electric power suppliers to energize the electronic products, it is essentially accompanied the electric power lines jangle, which leads to SAR problems.

One of the solutions of this electromagnetic compatibility problem in the human life environment is to work out the cordless contactless power suppliers having low SAR level.

This paper concerns with development of a transformer composed of the separated primary and secondary cores by air gap. Further, this paper is one of the success research solutions to overcome the SAR problem based on the finite elements and linear programming optimization methodologies. Namely, a contactless flat shaped transformer whose primal and secondary ferrite cores are separated has been successfully developed by the modern numerical computation approaches.

To realize the contactless transformer exhibiting low SAR level, we employ flat shape primal and secondary ferrite cores. Also, to obtain a high efficiency, we employ a secondary resonant circuit between the secondary leakage inductance and externally attached capacitor [1].

This transformer having the open magnetic flux paths between the primary and secondary core is of the paramount important part to realize the contact-less power suppliers.

Previously, we have reported that an application of the discrete wavelets transform to the magnetic field vector distributions around the transformer having open magnetic flux paths clarifies that the soup plate like ferrite cores embedding spirally wound coils gives a far excellent magnetic field vector distribution compared with those of the conventional U shape cores. Further, it has been revealed that

the flat transformer employing soup plate shape ferrite cores and spirally wound coils confines the magnetic fields at the center of the flat transformer, which minimizes the magnetic fields around the transformer [2,3].

In this paper, we have carried out an intensive finite elements simulation to evaluate the leakage magnetic fluxes, and to optimize the core size, core shape, number of turns, diameter of conductor and the circuit parameters of the transformer. As a result, it is revealed that numerical and experimental studies employing a secondary resonant technique reveal that our flat transformer with 1cm air gap and 0.69 coupling factor is capable of transmitting 79 percent of the input power to the secondary circuits [4].

IX. FUNDAMENTAL CHARACTERISTICS

1) Core shape design

In the contactless power suppliers, the primal and secondary distinct magnetic cores are always used to transmit electric power through air gap. Further, high frequency drive of the transformer is always employed in order to reduce the weight of the magnetic cores.



Fig. 1 A tested soup plate like ferrite core transformer.

One of the magnetic materials having good high frequency characteristic is a ferrite so that our contactless transformer has employed the two distinct flat shape ferrites as shown in

Fig.1. The primal and secondary magnetic cores are the same core whose shape is like a soup plate filling up the spirally wound coils instead of soup. To evaluate the optimum core size, number of turns, and the circuit parameters of the transformer, we have carried out an intensive finite elements simulation.

2) *The magnetic field vector distribution*

Fig.2 shows a measured magnetic field vectors distribution at some instance of the tested flat transformer under the 1Ω pure resistive load and secondary resonant conditions.

Although a relatively large air gap of 1cm between the primary and the secondary cores, Fig.2 reveals that major magnetic fluxes are concentrated at the center of flat cores. This suggests that our flat cores keep the leakage magnetic fluxes in small, i.e., keep the low level of SAR.

Further, it has been possible to observe the significant magnetic field vectors as shown in Fig.2, even though magnetic fields caused by the secondary load current cancel the primal magnetic fields.

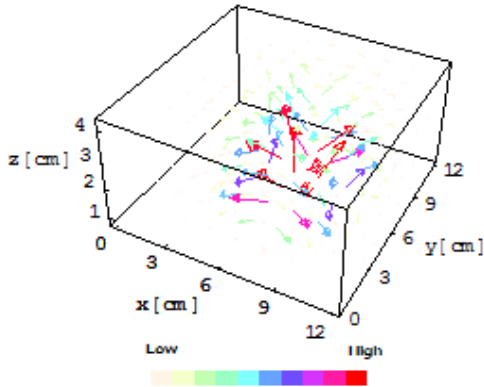


Fig.2 Magnetic field vector distribution of the tested transformer under the 1Ω pure resistive load and secondary resonant conditions.

3) *Coupling factor*

A coupling factor κ is one of the most important transformer characteristics, which indicates smallness of the leakage magnetic field vectors between the primary and secondary coils. Namely, as possible as large coupling factor κ means as possible as small leakage magnetic field vector distribution around the transformer.

Let us consider a simplified circuit model of the transformer shown in Fig. 3 to evaluate the coupling factor κ . The dots '.' shown over the primary and secondary coils in Fig.3 indicate the positive induced voltages at each of the coil terminals.

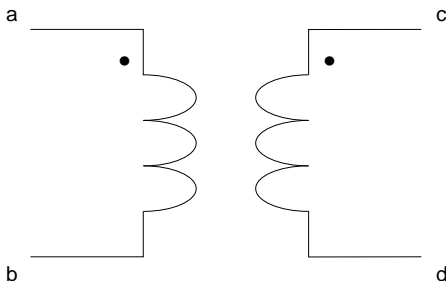


Fig.3 Simplified circuit model of a transformer to evaluate the coupling factor κ .

When we connect each of the terminals in Fig.3 to additive polarity as shown in Fig. 4(a), it is possible to obtain the following relationship

$$L_a = L_1 + L_2 + 2M \quad (1)$$

where L_a , L_1 , L_2 and M are the additive-, primary self-, secondary self- and mutual inductances, respectively.

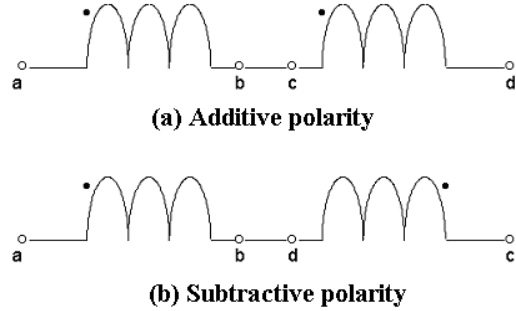


Fig.4 Series connection of the primary and secondary coils in Fig. 3.

Also, when we connects each of the terminals in Fig. 3 to subtractive polarity as shown in Fig. 4(b), we have

$$L_s = L_1 + L_2 - 2M \quad (2)$$

where L_s is a subtractive-inductance.

Further, the primary and secondary self-inductances can be measured independently. Thereby, combination of (1) and (2) leads to the mutual inductance M and coupling factor, which are respectively given by the following equations

$$M = \frac{L_a - L_s}{4},$$

$$k = \frac{M}{\sqrt{L_1 L_2}}. \quad (3)$$

Table 1 lists the measured inductances L_a , L_s , L_1 , L_2 and coupling factor κ changing the air-gap length between the primary and secondary core surfaces.

TABLE I Coupling factor of the tested transformer employing flat shape cores measured at 30kHz.

Gap[mm]	0	1	3	5	7	10
L_1 [μH]	578.6	348.2	231.1	181.6	169.9	133.9
L_2 [μH]	572.7	348.1	229.4	181.0	168.3	133.3
L_s [μH]	2297.4	1358.2	881.8	669.4	617.6	450.8
L_o [μH]	16.9	26.1	41.4	56.0	61.1	84.3
K	0.99	0.96	0.91	0.84	0.82	0.69

The results listed in Table 3 suggest that the tested transformer is capable of keeping the good coupling factors $\kappa \approx 0.7$, even if the primary and secondary coils are separated by air-gap of 1cm.

4) Power transmission rate

Power transmission rate is the other important characteristic, which indicates the efficiency of the transformer.

To improve the transformer efficiency, a secondary resonance between the capacitor and secondary leakage inductance is widely used and well known technique [4].

Fig.5 shows a simplified circuit model attaching a resonant capacitor C.

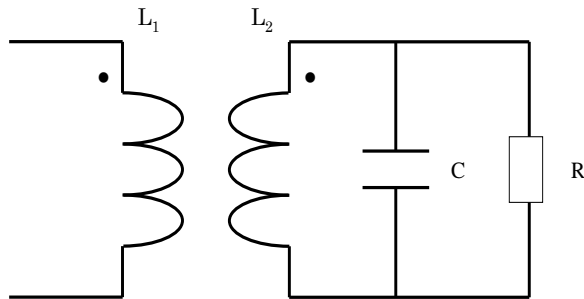


Fig. 5 Circuit diagram model of a secondary resonant type transformer.

Attaching 40 μ F resonant capacitor in parallel to the secondary coil terminal of the tested transformer leads to a nearly $\varepsilon \approx 80\%$ input power transmission rate defined by

$$\varepsilon = \frac{\text{Secondary output power}}{\text{Primary input power}} \times 100 [\%] \quad (4)$$

X. THE FINITE ELEMENTS AND OPTIMIZATION

1) The finite elements simulation

We have carried out an intensive finite elements simulation to evaluate the leakage magnetic fluxes, and to optimally design the core size, core shape, number of turns, diameter of conductor and the circuit parameters of the tested transformer.

This numerical simulation has been carried out by a free finite element software FEMM (Finite Element Method Magnetics). Fig.6 shows a cross-section of the simulation model.

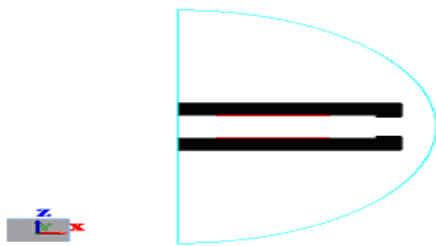


Fig.6 Tested transformer employing the soup plate like ferrite cores.

Fig.7 shows the primal self-inductance changes in accordance with the air-gap length changing between the primary and secondary core surfaces. The results in Fig.7

suggest that computed and experimented primal self-inductances exhibit the similar tendency to the change of air-gap length. Thus, it has been shown that the simulation model in Fig. 6 is well corresponding to the practical one. Fig.8 shows one of the magnetic flux density distributions around the tested transformer.

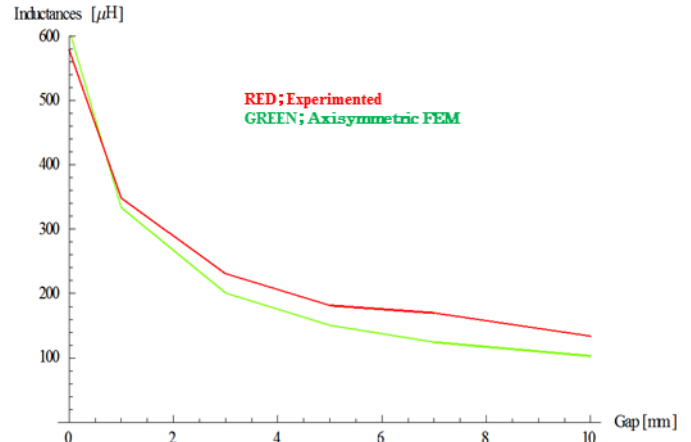


Fig.7 The computed primal self-inductances along with the measured ones.

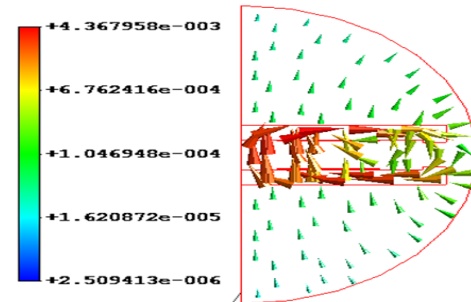


Fig.8 Magnetic field vectors distributions around the tested transformer. Color bar unit is tesla.

1) Linear programming optimization

The power transmission rate from the entire primary input to the secondary output powers of the transformer is defined by (4). By utilizing the circuit parameters, e.g., inductances obtained by the finite elements simulations, the linear programming optimization of (4) with respect of frequency and capacitance yields a result shown in Fig.9.

The results in Fig.9 suggest that our contactless transformer having a relatively large 1cm air gap is capable of obtaining over 80% efficiency ε . This result by numerical optimization method was verified by the practical experiments as described in 2.4 of this paper. Thus, we have succeeded to demonstrate the usefulness and validities of modern computational approach to the electrical device design.

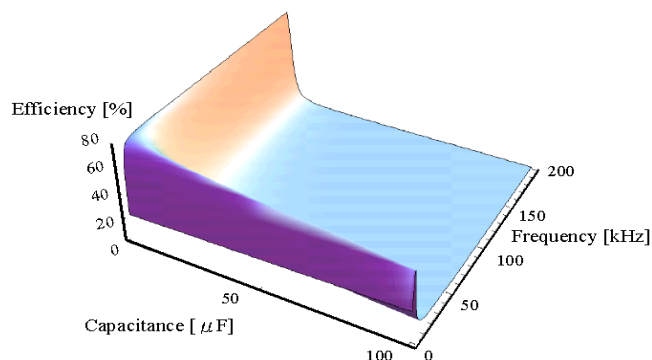


Fig.9 Power transmission efficiency evaluated by the linear programming optimization.

XI. CONCLUSION

To realize the contactless transformer exhibiting low SAR, this paper has worked out one of the reasonable transformers having open magnetic flux path by means of the finite elements approach.

Our proposed transformer suppresses the leakage magnetic fields around the core, because it is a natural extension of the shell type core structure. Thus, we have succeeded in demonstrating not only the usefulness and validities of modern computational approach to the electrical device design but also working out the optimum discrete core transformer.

REFERENCES

- [8] S.Takada, Y.Saito and K.Horii, Visualization of the magnetic field vectors around the contact-less power suppliers, Japan Society of Visualization, Proceedings of the Visualization Symposium in 2000, Paper No. P01-001.
- [9] S.Matsuyama, S.Matsuyama, Y.Saito, Data Handling Methodology for Discrete Wavelets and Its Application to The Dynamic Vector Fields, International Journal of Wavelets, Multiresolution and Information Processing, Vol.4, No.2, June (2006) pp.263-271. World Scientific Publishing Company.
- [10] S.Matsuyama, Y.Oguchi, Y.Saito, T.L.Kunii, Handling Technique of the Dynamic Color Computer Graphics by the Wavelets transform, Japan Society of Visualization, Proceedings of the Visualization Symposium in 1999, Paper No. 206.
- [11] J.L. Harrison, A new resonance transformer, Electron Devices, IEEE Transactions on Issue Date: Oct 1979 Vol.26 Issue: 10, pp. 1545 - 1